Journal of Energy Storage 55 (2022) 105824

Contents lists available at ScienceDirect

Journal of Energy Storage

journal homepage: www.elsevier.com/locate/est

Research papers

Corrosion performance of alloy 800H and alloy 625 for potential use as molten salts solar receiver materials in concentrating solar power tower plants

Cristina Prieto [a,b], F. Javier Ruiz-Cabañas [a], Virginia Madina [c], A. Inés Fernández [d], Luisa F. Cabeza [e,*]

[a] Abengoa Energía, Solar Technology Department, Energía Solar 1, 41014 Sevilla, Spain
[b] Department of Energy Engineering, Universidad de Sevilla, Camino de los Descubrimiento s/n, 41092, Spain
[c] Materials and Processes Area, Tecnalia Research and Innovation, Mikeletegi Pasealekua, 2, 20009 San Sebastián, Spain
[d] Department of Materials Science & Physical Chemistry, Universitat de Barcelona, Martí i Franqués 1-11, 08028 Barcelona, Spain
[e] GREiA Research Group, INSPIRES Research Centre, Universitat de Lleida, Pere de Cabrera s/n, Lleida, Spain

ARTICLE INFO

Keywords:
Corrosion
Molten nitrate salt
Alloy 625
Alloy 800H
Solar receiver

ABSTRACT

Two high corrosion resistant super-alloys, alloy 800H and alloy 625, were evaluated for corrosion compatibility with molten nitrate salts at 565 °C under air atmosphere since these super-alloys are possible candidates for the manufacturing of molten salts solar receivers in the CSP tower technology. Both alloys are tested in two different molten nitrate salts grades to identify how the impurities of the final mixture affect to corrosion damage. Accordingly, a technical grade molten nitrate salt (Solar_Salt_T) and refined molten nitrate salt (Solar_Salt_R) are selected as test media. In addition to corrosion rates calculation, techniques such as XRD, EDS, optical and scanning electron microscopy are used to identify the corrosion morphology and oxides layers chemistry. Alloy 800H and alloy 625 show uniform corrosion after testing without detecting localized phenomena such as pitting, stress corrosion cracking, crevice, or intergranular corrosion. While alloy 800H develops a duplex oxide layer consisting of iron oxides in its external part, and chromium oxide in its innermost layer, alloy 625 generates a compact and highly adherent oxide layer consisting mainly of nickel oxide. Corrosion rates decrease with time, being higher for alloys exposed to Solar_Salt_T mixtures. Moreover, alloy 625 shows lower corrosion rates than alloy 800H in all conditions tested in this study.

1. Introduction

Carbon dioxide is responsible of over 60 % of greenhouse gas (GHG) worldwide emissions [1–3], being the largest contributor factor to climate change. Demand of energy has significantly increased recently due to the growth of worldwide population and high industrialization. This growth occurs mainly in emerging countries, increasing significantly the need of new generation plants, while in developed countries the increase in energy demand is related to replacement of end-of-life existing power plants. Renewable energy sources have been a key player to contribute to the world CO_2 greenhouse gas emission reduction [4]. Solar energy is the most abundant renewable source by far, and just 0.1 % of the solar energy reaching the surface of the earth would be enough to cover the worldwide needs (considering 10 % efficiency conversion). Accordingly, Concentrated Solar Power (CSP) technology is crucial for solving the global climate challenge due to following characteristics: (i) clean electricity supply and (ii) the capacity of integrating large scale thermal energy storage (TES) systems to adapt electricity production to daily energy demand [5–8].

Nowadays, the existing CSP technology with the perceived greatest potential in terms of cost/performance is the so-called Molten Salts Tower (MST) technology. MST technology uses a mixture of nitrate salts (60 wt% $NaNO_3$ + 40 wt% KNO_3, also called solar salt) as both heat transfer fluid (HTF) and storage fluid. This molten nitrate salt has a maximum operation temperature given by the decomposition of the nitrates around 565 °C, used to produce superheated steam for Rankine cycles [9–11]. Properties such as low vapor pressure, high energy density, high thermal stability, non-flammable, non-toxic performance and

* Corresponding author.
E-mail address: lcabeza@diei.udl.cat (L.F. Cabeza).

https://doi.org/10.1016/j.est.2022.105824
Received 14 February 2022; Received in revised form 9 September 2022; Accepted 3 October 2022
Available online 12 October 2022

low cost, make nitrates salts proper candidates for HTF and storage fluids [12,13]. Therefore, the use of nitrates salts with a direct storage system in MST plants is currently the most competitive CSP commercial solution.

The solar receiver is one of the most critical components in MST facilities, since this equipment is subjected to aggressive working conditions. The solar receiver is located on the top of the tower, and it is responsible of transferring the concentrated radiation from the solar field to the molten salts. Accordingly, the solar receiver is exposed to high peak fluxes (higher than 1000 suns) which imply extreme thermal-mechanical loads over this component during the life of the plant. Therefore, many efforts have been focused on optimizing the thermal and mechanical performance of this equipment during the last years [14–16]. In addition to these challenges, molten salts corrosiveness is one of the most important drawbacks inherent to this fluid at high temperature, being a critical factor to consider during the design of commercial solar receivers. High temperature nitrates in combination with the solar receiver metal alloy constitute a corrosive system, with the molten salts acting as an electrolyte. Molten salts corrosion mechanism is driven by two main stages. First, an alloy oxidation phenomenon. This phenomenon generates the corresponding oxides layers, depending on the alloying elements of the metal and molten salts nature. Subsequently, molten salt produces a fluxing action over the protective oxide layers, deteriorating it by dissolution. Therefore, the transference of oxidizing species through the metal and from the metal ions into the molten salt is favored, initiating an accelerated attack [17]. Then, the use of inappropriate materials selection for the solar receiver could result in the deterioration of the alloy, compromising the lifetime of this component and finally the performance of the MST plant.

Common materials such as carbon steel or stainless steel are thoroughly researched and commercially used as materials for the molten salts storage system. Nevertheless, solar receivers work under different thermo-mechanical conditions, mainly due to the required pressure levels (around 3 bar). These thermo-mechanical requirements coupled with nitrate salts corrosion compatibility make high corrosion resistant super-alloys the main candidates for the manufacturing of molten salts solar receivers [18]. Corrosion performance of high strength and corrosion resistant alloys in contact with high temperature nitrates salts have been evaluated in the state-of-the-art by different authors. Kruizenga et al. [19] evaluated the corrosion performance of alloy 625 and alloy 230 in contact with molten nitrate salts at different temperatures: 400 °C, 500 °C, and 680 °C. Corrosion at 400 °C and 500 °C was low for both alloys (between 0.2 and 1.8 μm/year) due to the development of protective NiO oxide layers. On the other hand, corrosion at 680 °C was significant, as metal wastage occurred (measured corrosion rate between 594 and 688 μm/year). Additional corrosion tests were carried out by Kruizenga et al. [20] at 600 °C, over thirteen materials involving Fe-Cr-Ni, Fe-Ni-Cr, Ni-Fe-Cr and Ni-Cr/Mo alloys, such as stainless steels (321 and 347), 214, 224, 230 and 625 alloys, among others. Federsel et al. [21] analyzed the corrosion performance of 321 stainless steel and alloy 600 in contact with Hitec salt (40 wt% $NaNO_2$ + 53 wt% KNO_3 + 7 wt% $NaNO_3$) at 530 °C discussing the importance of parameters such as oxide ion concentration, cover gas and chlorides concentration in corrosion phenomena. Moreover, Zhang et al. [22] tested the corrosion behavior of alloy 800H as candidate for solar receiver tube material in molten nitrate salts at 560 °C for short test times (5 h, 10 h, 20 h, 30 h, 40 h, 60 h, and 80 h) measuring corrosion rates in the range of 91.5 μm/yr. In addition, alloy 800H was also analyzed by Bradshaw et al. [23] using a thermal convection loop that operated between 300 °C and 600 °C using molten nitrate salts as heat transfer fluid.

Two different alloys, alloy 625 (UNS N06625) and alloy 800H (UNS N08810) are selected to validate the corrosion performance after the exposure at high temperature (565 °C) of the nitrates salts. Alloy 625 is a high strength and corrosion resistant nickel-chromium alloy showing an excellent workability. Alloy 625 strength is derived from the stiffening effect of molybdenum and niobium on nickel-chromium matrix. The presence of these elements is also responsible for the excellent corrosion performance for many different environments in a wide range of temperature. Typical application for alloy 625 are petrochemical, nuclear, seawater components and aircraft ducting systems among others. On the other hand, alloy 800H is a high temperature strength nickel-iron alloy, with outstanding resistance to oxidation, carburization and other types of high temperature corrosion. Carbon content range associated to alloy 800H and annealing treatments grants high creep resistance and good rupture properties. Alloy 800H has been extensively used for high corrosion and heat resistant applications, such as petrochemical and chemical processing, pressure vessels, heat exchangers and hydrocarbon cracking among others. Both materials have been proposed for the construction of current and advanced molten salts solar receivers [18,24–27].

Therefore, the tests matrix designed within this study try to cover parameters (such as alloying metal, test time, salt purity, and different types of corrosion attacks) needed to identify if these alloys are good candidates from corrosion point of view for the proposed application. The aim of this study is to cover some gaps found in the literature, such as the comparative performance of these alloys in different molten salts purities and the analysis of localized phenomena, stress corrosion cracking (SCC), and crevice corrosion. The exposure times, 500 h and 1470 h, considered by the authors are significantly enough to enrich the state-of-the-art in this field.

The laboratory tests performed face the following purposes:

(i) To quantify corrosion rates associated to alloy 800H and alloy 625 under test conditions.
(ii) To identify if these alloys are susceptible to localized phenomena such as SCC, crevice and intergranular corrosion.
(iii) To discuss about the importance of corrosion products chemistry in the corrosion resistance of the alloys.
(iv) To analyze the corrosion performance evolution as a function of time, estimating the behavior of both alloys for long-term expositions.
(v) To evaluate the effect of molten nitrate salts impurity level over fluid aggressiveness in terms of corrosion.

2. Materials and methods

2.1. Nitrates salts

A binary mixture of nitrate salts consisting of 60 wt% $NaNO_3$ and 40 wt% KNO_3 and melting point 230 °C, is used to evaluate the corrosion performance of the metal alloys under evaluation in this study. As described previously, this nitrate salts mixture is the so-called "Solar salt". Two different grades, technical and refined, were provided by SQM for each constituent ($NaNO_3$ and KNO_3). Purity and main impurities associated to each grade are described in Table 1. In order to evaluate how the impurities affect to the corrosion performance at 565 °C, two mixtures are prepared: (i) Solar_Salt_T, 60 wt% Technical $NaNO_3$–40 wt% Technical KNO_3, and (ii) Solar_Salt_R, 60 wt% Refined $NaNO_3$–40 wt% Refined KNO_3.

The chloride content of solar salts is one of the main limitations in the use of said salts at high temperatures. Prieto et al. [28] evaluated how the chloride content increases the corrosion rate and influences the scale produced at 400 °C (Table 2).

This study shows that the higher is the content of chloride in molten salts the greater is the steel loss produced by corrosion and makes the corrosive kinetics to be highly increased when it is overtake at 565 °C.

2.2. Metal alloys

Table 3 shows the expected chemical composition, according to the standard [29], and the composition from the material certificate issued by the supplier for alloy 625 and alloy 800H.

Table 1
$NaNO_3$ and KNO_3 purity and impurities.

Salt	Grade	Purity and impurities (wt%)						
		Purity	Chloride	Magnesium	Nitrite	Sulfate	Carbonate	Hydroxil
$NaNO_3$	Technical	99.2	0.21	0.035	0.02	0.10	0.10	0.20
$NaNO_3$	Refined	99.5	0.10	0.02	0.02	0.10	0.10	0.20
KNO_3	Technical	99.3	0.20	0.02	0.02	0.10	0.10	0.20
KNO_3	Refined	99.6	0.10	0.01	0.02	0.05	0.02	0.01

Table 2
Final chloride Cl- content.

Final mixture	$[Cl^-]$ (%w)
60%$NaNO_3$ SQM technical grade + 40%KNO_3 technical grade	0.103
60%$NaNO_3$ SQM refined grade + 40%KNO_3 refined grade	0.042

A microscopic examination is carried out over both materials on reception, to analyze the microstructural characteristics of both alloys. This evaluation is done using a Motic BA210 trinocular compound microscope. To this end, several sections are cut from the plates and embedded in resin as a preparation for later characterization. Alloy 800H shows an austenitic microstructure consisting of equiaxial grains whose size are in the range 2–3, according to ASTM-E112 (Fig. 1a and b) [30]. Titanium carbide/nitrides precipitates are also found in the matrix. Alloy 625 also shows an austenitic microstructure with a significantly smaller grain size; greater than 8 (Fig. 1c and d). The scale used for grain measurement can be found in ASTM-E112 [30].

2.3. Methodology

To analyze the corrosion performance evolution for both metal alloys, immersion corrosion tests are designed using Solar_Salt_T and Solar_Salt_R mixtures as test media. The duration of these test is

Table 3
Alloy 800H and alloy 625 chemical composition [29].

Alloy	UNS		Chemical composition (wt%)										
			Ni	Mo	Cr	Fe	Co	Nb	Mn	Si	C	Al	Ti	Others
800H	N08810	Standard	30.0–35.0	–	19.0–23.0	39.5[b]	–	–	1.5[a]	1.0[a]	0.06-0.10	0.15-0.60	0.15–0.60	Cu: 0.75[a]
		Material certificate	30.55		20.59	46.77	0.04	0.01	0.70	0.42	0.08	0.28	0.32	Cu: 0.04
625	N06625	Standard	58.0[b]	8.0-10.0	20.0-23.0	5.0[a]	1.0[a]	3.15-4.15	0.50[a]	0.50[a]	0.10[a]	0.40[a]	0.40[a]	
		Material certificate	62.08	8.7	21.1	3.8	0.06	3.47	0.03	0.19	0.02	0.18	0.20	Cu: 0.01 Ta: 0.01

[a] If only one value is given, value shows maximum percentage.
[b] Minimum value for this alloying element.

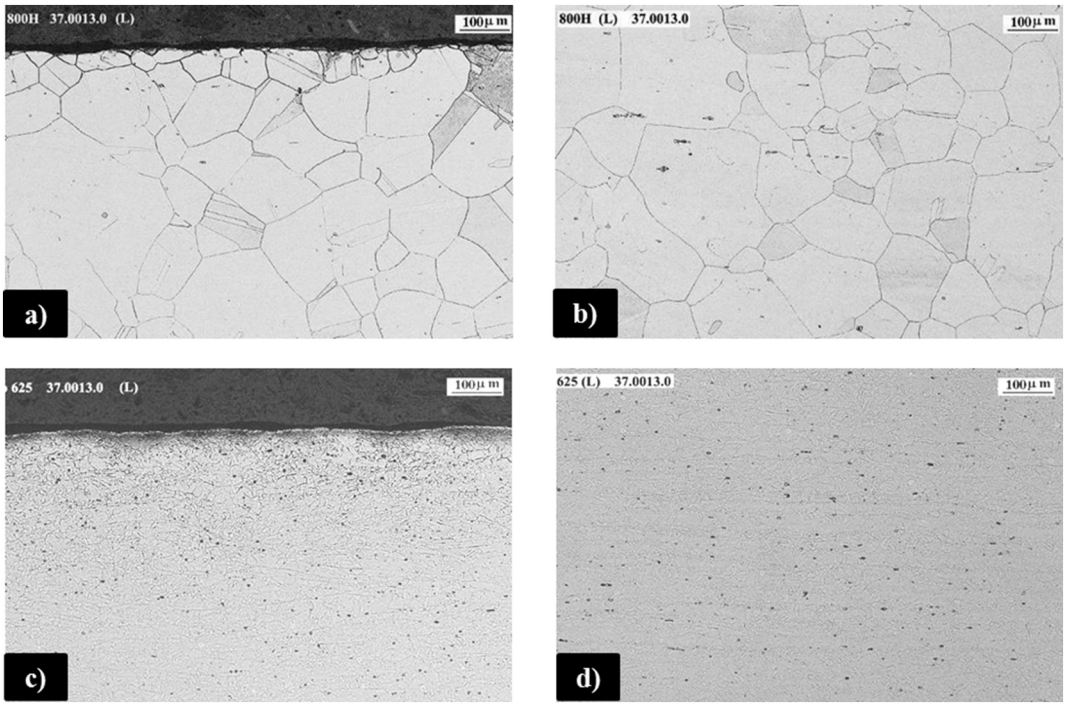

Fig. 1. Alloys microstructure on reception. (a) and (b): Alloy 800H; (c) and (d): Alloy 625.

stablished as 500 h (t_1) and 1470 h (t_2). To obtain Solar_Salt_T and Solar_Salt_R mixtures, technical and refined sodium and potassium nitrates salts are weighted and blended in 316 L stainless steel crucibles Previous laboratory tests and several research studies have shown for 316 L stainless steel a good corrosion resistance in nitrate molten salts at temperatures up to 570 °C [31,32]. In these documents the corrosion tests in molten nitrate salts were also carried out in 316 crucibles. Then, the crucibles are introduced in a furnace to carry out the melting process. Once melted, the corrosion coupons are introduced in the salt and the temperature is increased up to 565 °C (Fig. 2).

Metallic plates from ThyssenKrupp measuring 250 × 250 × 2 mm are used to machine two different types of metallic corrosion coupons: uniform corrosion coupons and U-bend specimens (Fig. 3). Rectangular uniform corrosion coupons are cut from the main plates, and a hole (10 mm diameter) is drilled in the upper side of each coupon. Suitably washers are used to avoid galvanic corrosion phenomena when the uniform corrosion coupons are hung in the 316 L stainless steel tree device used for testing (Fig. 4a and b). These types of coupons are used to calculate corrosion rates experienced by both alloys attending to ASTM G1-03 standard [33]. Once machined and before testing, uniform corrosion coupons are weighted. In this manner, weight losses associated to each material after testing can be calculated after the oxide layers are removed using an adequate chemical etching. The cleaning chemical solution used to remove the oxides layer generated during the thermal-corrosive treatment is extracted from ASM specialty handbook [29]. The descaling process proposed to ensure the removal of the complete oxide without affecting the base metal is composed of two consecutive stages: (i) 1–2 h immersion in the solution 15 wt% NaOH +5 wt% $KMnO_4$ (rest H_2O) at 80 °C and (ii) immersion in the solution 20 wt% HNO_3 + 2 wt% HF (rest H_2O) at 50 °C. ASTM G1–03 proposes the following equation to obtain the corrosion rates as μm/year:

$$Vc = \frac{\Delta W}{S_0}\frac{K}{t\rho} \quad (1)$$

In this equation, ΔW is the weight loss of the coupon after the test and the removal of the oxide layers (g). S_0 is the initial metallic surface in contact with the nitrates salts (cm^2) K is a constant to express the final result as μm/year (8.76×10^7), and *t* is the test time in hours and ρ is the metallic alloy density in g/cm^3. It is assumed that the total weight loss measured after descaling is due only to generalized corrosion and not produced by localized phenomena such as pitting corrosion or other corrosion attacks over the alloy. At least two coupons for each material and test medium are used to obtain corrosion rates, calculated as the average value among results. In addition to calculate corrosion rates, uniform corrosion coupons are also used to evaluate the morphology and extension of the corrosion damage by optical and electron microscopy over metallographic specimens (Motic BA210 trinocular compound microscope and SEM-JEOL 5910-LV microscope). Corrosion products chemical composition is analyzed by energy dispersive spectroscopy (EDS) using a microanalyzer (EDS-OXFORD INCAx-act) coupled to SEM. Finally, X-Ray diffraction (XRD) is used to identify oxides stoichiometry (Bruker D8 Advance XRD).

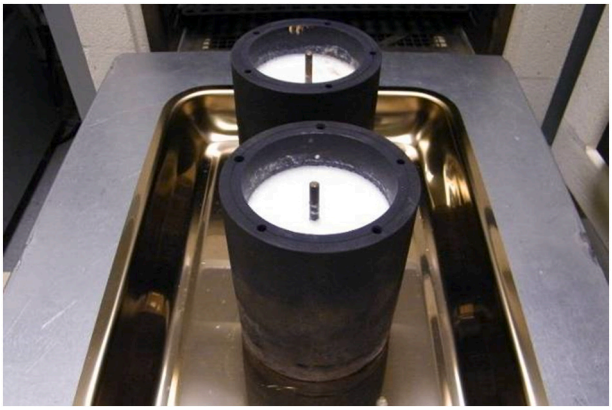

Fig. 2. Crucibles containing molten nitrate salt and corrosion coupons.

On the other hand, SCC specimens are shaped by bending rectangular coupons extracted from the metallic plates following guidelines described in ASTM G30–97 standard [34]. In this way, specimens are bended at 180° to produce plastic deformation over the material. This deformation level and associated residual stresses is maintained during the corrosion tests by the use of screws with nuts and washers (Fig. 4a and b). In addition to SCC susceptibility, crevice corrosion is also evaluated by using alumina washers located in the straight zone of the U-bend specimens (Fig. 4b). The ceramic device creates an overlapped area where crevice corrosion is analyzed, following indications extracted from ASTM G-78 standard [35]. Three U-bend coupons are used for each alloy and test fluid during the second test time (t_2, 1470 h) to evaluate the resistance of both alloys to SCC and crevice corrosion phenomena.

3. Results and discussion

3.1. Visual inspection

Once corrosion tests are finished, t_1 test time at 500 h and t_2 test time at 1470 h, the metallic tree devices are extracted from the crucibles with the salt still molten (Fig. 5). Metallic tree devices are introduced in an ultrasound bath with distilled water at room temperature to remove nitrates salts adhered to the metallic surfaces. Then, uniform corrosion and U-bend specimens are dried with alcohol and stored in a desiccator until they are examined.

3.1.1. Alloy 800H

All alloy 800H coupons show a uniform generalized corrosion with the formation of blackish-brown oxide layers, as observed in Fig. 6 (coupons after t_1 exposure) and Fig. 7 (coupons after t_2 exposure). Localized corrosion attack such as pitting corrosion is not observed in any corrosion coupons after testing (neither t_1 or t_2 test times). Secondly, oxide layers generated over corrosion coupons tested in Solar_Salt_R seem apparently more compact and better adhered than corrosion products developed by specimens tested in Solar_Salt_T (Figs. 6 and 7). Visual inspection and low magnification analysis (40×) shows no evidence of cracking in the U-bend specimens after t_2 test time (Fig. 7b and d). Finally, crevice corrosion is not observed once ceramic washers are removed from U-bend specimens (Fig. 7b and d). As a summary, no big differences are found between all coupons tested in Solar_Salt_R and Solar_Salt_T for both test times after visual inspection.

3.1.2. Alloy 625

Alloy 625 also shows uniform corrosion with blackish-brown corrosion products generation. Moreover, oxides layers seems compact and well adhered to the base metal (Figs. 8 and 9). Although no significant differences are detected in the corrosion morphology for coupons tested in Solar_Salt_R and Solar_Salt_T mixtures, corrosion extent in alloy 625 is lower than the observed in alloy 800H. Corrosion crevice attack and susceptibility to SCC are not observed for alloy 625 coupons in any test condition after 1470 h. In this way, no cracks are found in the bending area of U-bend specimens (Fig. 9b and d) nor damage in the overlapping areas under the ceramic devices (Fig. 9e).

3.2. Oxides layers chemical characterization

Chemical characterization of the corrosion products generated by alloy 800H and alloy 625 coupons during the test in both salts mixtures is analyzed by SEM-EDS and XRD. Oxides layers evaluation is focused on corrosion coupons tested in t_2 test time (1470 h). Major components and phases of the corrosion products are characterized by using these two techniques.

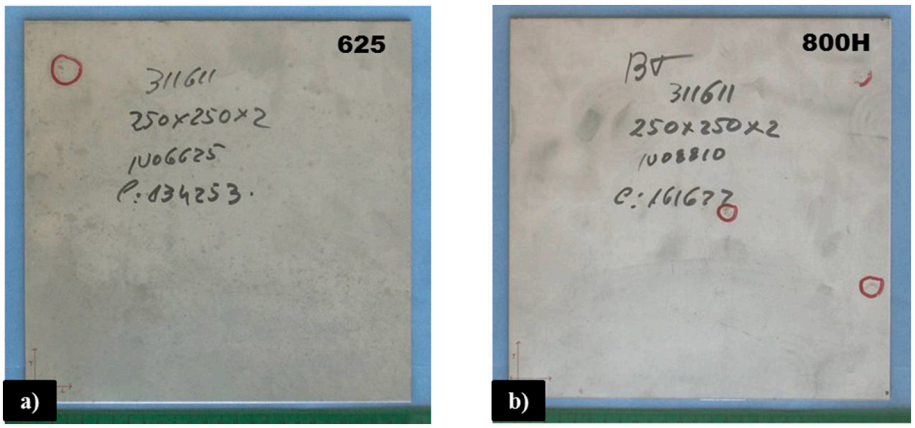

Fig. 3. Metal plates provided by ThyssenKrupp. (a) Alloy 625; (b) Alloy 800H.

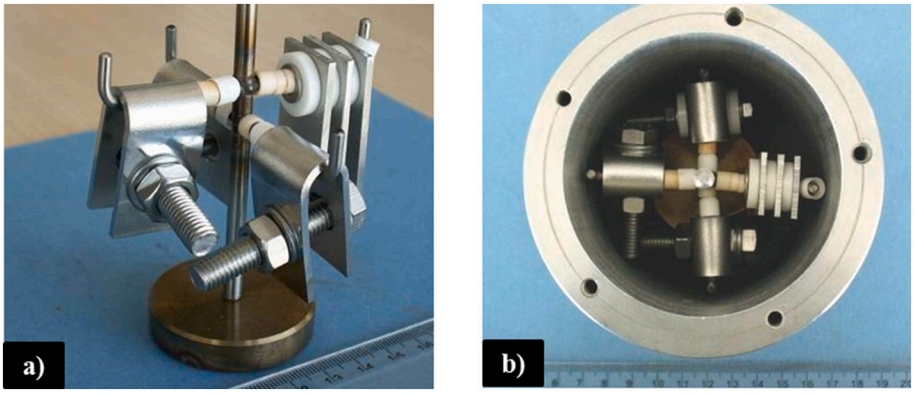

Fig. 4. Corrosion coupons assembly. (a) Coupons assembled into metallic tree device; (b) Metallic tree device with coupons inside the crucible.

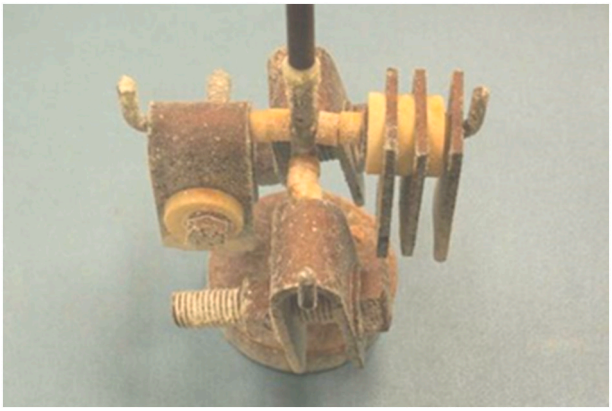

Fig. 5. Metallic tree device with uniform corrosion coupons and SCC specimens after testing.

3.2.1. Alloy 800H

Fig. 10 shows several SEM micrographs associated to alloy 800H. In this figure, corrosion products generated by this alloy after Solar_Salt_T (Fig. 10a) and Solar_Salt_R (Fig. 10b) mixtures exposure can be seen. EDS spectra for coupons exposed to Solar_Salt_T reveals that the external layer is mainly composed by iron (Fe) and oxygen (O) (Fig. 10d). Moreover, there are some areas where the oxide layer is spalled and broken, showing an innermost corrosion product where chromium (Cr) and nickel (Ni) are also detected (Fig. 10c). On the other hand, coupons exposed to Solar_Salt_R show a somewhat more heterogeneous layer (Fig. 10e). In addition to Fe and O, EDS analysis within this layer detected small amounts of calcium (Ca) and magnesium (Mg) (Fig. 10f).

Oxides layer chemical composition for coupons exposed to Solar_Salt_T is evaluated in more detail by using EDS mapping, to try to identify which type of oxides layers are generated after the thermal-corrosive treatments. Fig. 11 shows the coupon transversal section under evaluation, and the alloying elements distribution previously discussed. Results indicate that the outermost oxide layer is mainly composed of Fe and O, as iron oxide (Fig. 11c and e). On the other hand, the inner layer is fundamentally constituted by O and Cr (Fig. 11b and e), as chromium oxide. XRD is used to analyze the stoichiometry of the external corrosion products, obtaining two different iron oxides as main constituents: magnetite (Fe_3O_4) and hematite (Fe_2O_3) (Fig. 11f).

3.2.2. Alloy 625

Alloy 625 surface SEM analysis shows a crystalized oxide layer after it being exposed to both nitrates mixtures: Solar_Salt_R and Solar_Salt_T (Fig. 12a and b as detail of coupons tested in Solar_Salt_T). EDS spectra shows no significant differences between coupons tested in both salts, as alloying elements profiles are practically identical. Accordingly, corrosion products include an important presence of Ni and O, which is indicative of nickel oxides formation (Fig. 12c and d). In addition to Fe, Cr, Ni and O, EDS also shows the presence of magnesium, which is an impurity in Solar_Salt_R and Solar_Salt_T mixtures [36]. This element tends to crystallize on the outer oxide layer. Finally, a more detailed analysis of the oxide layers stoichiometry is performed by using XRD, exposing nickel oxide as NiO as expected by previous EDS analysis (Fig. 12e).

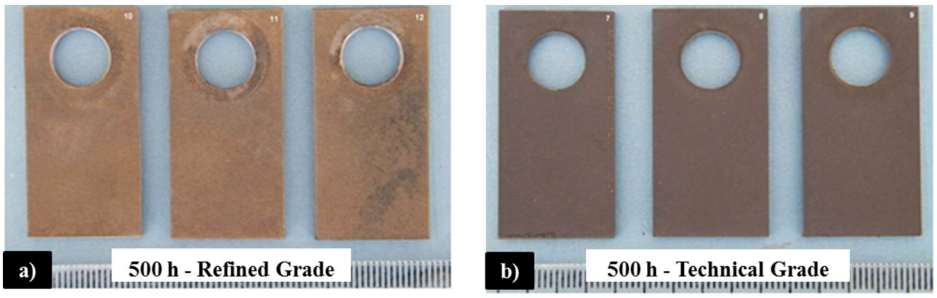

Fig. 6. Alloy 800H corrosion coupons after t_1 test time. (a) Solar_Salt_R; (b) Solar_Salt_T.

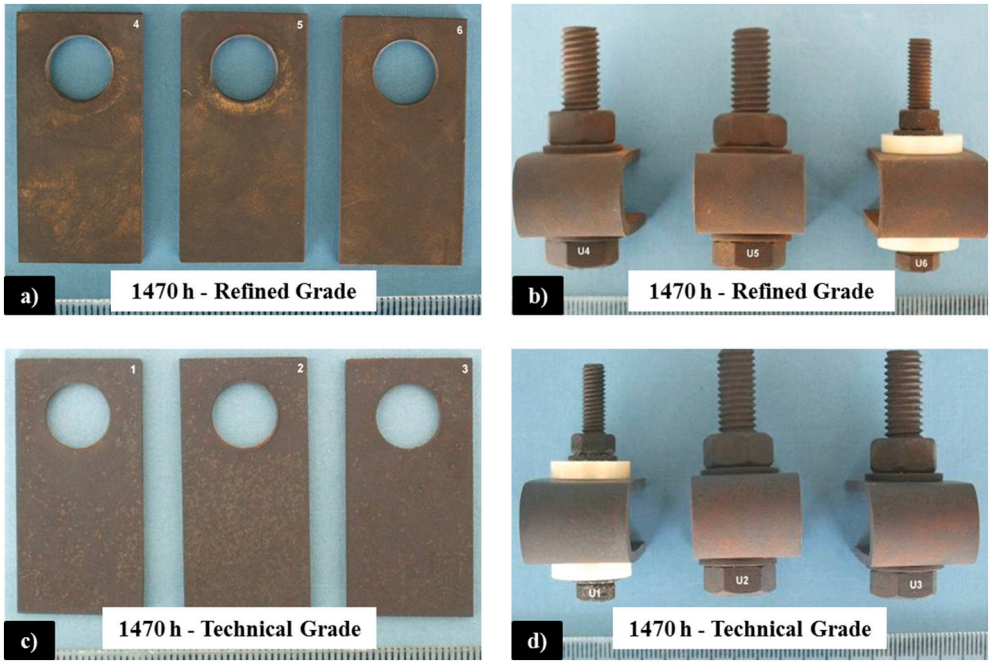

Fig. 7. Alloy 800H corrosion coupons after t_2 test time (before cleaning procedure). (a) Solar_Salt_R – Uniform corrosion coupons; (b) Solar_Salt_R – U-Bend specimens; (c) Solar_Salt_T – Uniform corrosion coupons; (d) Solar_Salt_T – U-Bend specimens.

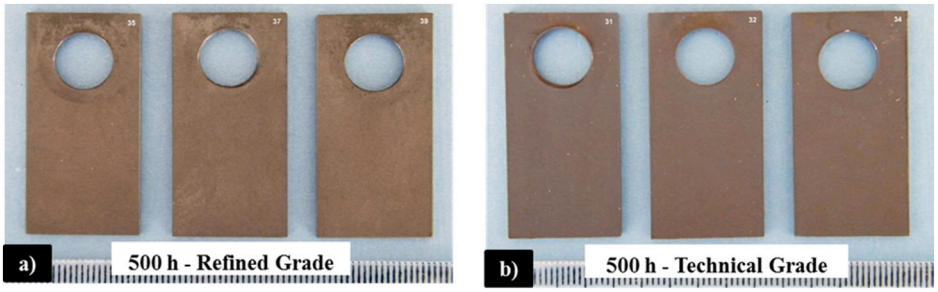

Fig. 8. Alloy 625 corrosion coupons after t1 test time. (a) Solar_Salt_R; (b) Solar_Salt_T.

3.3. Metallographic evaluation

Metallographic specimens are prepared from sections extracted from alloy 800H and alloy 625 uniform corrosion coupons. These sections are prepared for metallographic evaluation by embedding them in resin, and then polished to carry out the evaluation using optical microscopy and SEM. The main goal of this analysis is to evaluate the morphology and corrosion progress through the alloys under evaluation.

3.3.1. Alloy 800H

Optical micrographs displayed in Fig. 13 shows the duplex nature of the oxide layer generated over alloy 800H corrosion coupons tested in both test media, Solar_Salt_R (Fig. 13b and d) and Solar_Salt_T (Fig. 13a and c). Apparently, the outermost layer composed by iron oxides, grows outward while the innermost layer, composed by chromium oxide presents an inward growth through the base metal. The inner layer shows a more irregular growth, although the penetration depth is approximately constant. In general, the corrosion product is uniform in terms of maximum thickness and well adhered over the alloy. However, even

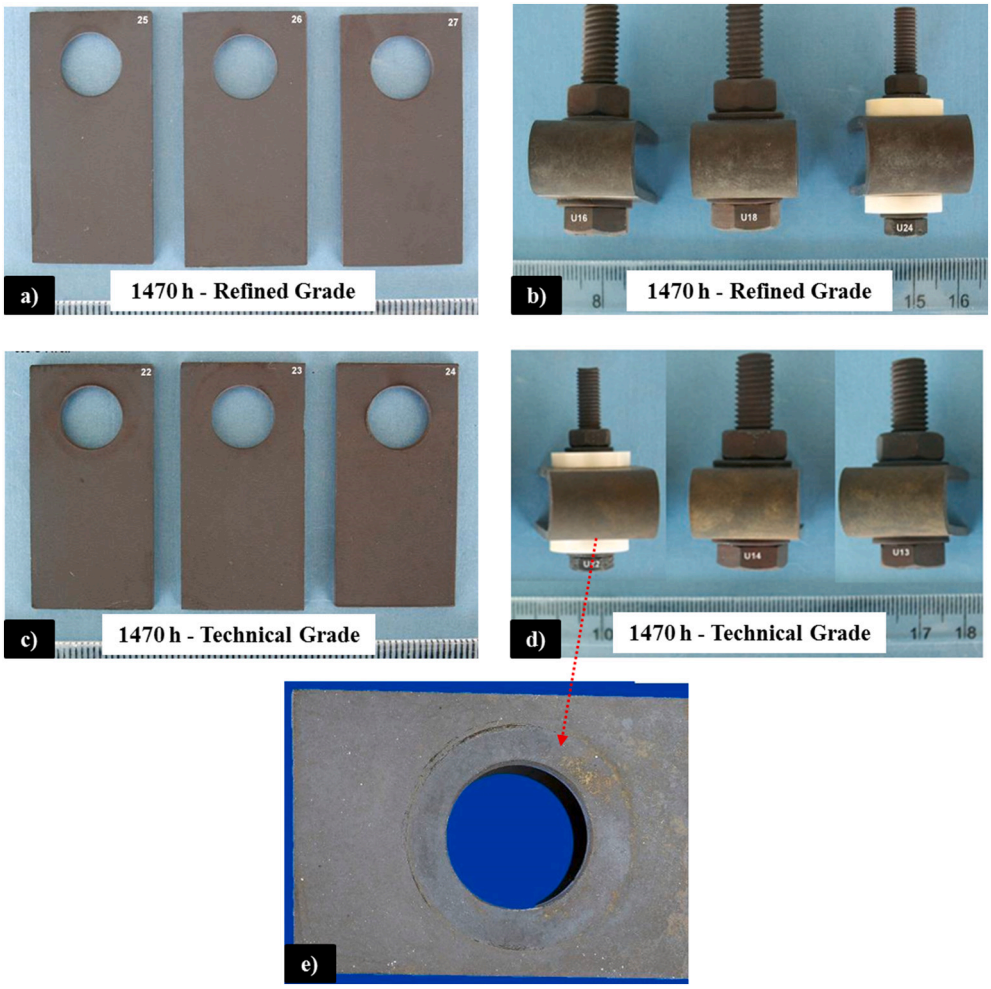

Fig. 9. Alloy 625 corrosion coupons after t2 test time. (a) Solar_Salt_R – Uniform corrosion coupons; (b) Solar_Salt_R – U-Bend specimens; (c) Solar_Salt_T – Uniform corrosion coupons; (d) Solar_Salt_T – U-Bend specimens; (e) Overlapping area detail.

though transversal metallographic evaluation shows a good adhesion between chromium oxide layer and base metal, surface analysis shows some spalling phenomena associated to external iron oxides after Solar_Salt_T mixture exposure (Fig. 10a). Some conclusions extracted from Fig. 13 are: (i) for the same test time, the oxide layer thickness is lower for coupons exposed to Solar_Salt_R mixture than for the tested in Solar_Salt_T, and thickness increase take place both in the outer layer as in the internal layer. (ii) For the same salt mixture, oxide layer thickness increases as the test time increases. (iii) No differences are observed between the morphology of the oxides layers generated after Solar_Salt_R and Solar_Salt_T exposure. Duplex oxide layer is detected for both test fluids with two separate oxides with individual growth kinetics, and (iv) metallographic etching shows a similar microstructure for alloy 800H to the non-tested material. Phenomena such as grain growth, intermetallic phases precipitation and intergranular oxidation are not detected after testing in any test condition (Fig. 14).

3.3.2. Alloy 625

Microstructure characterization carried out by SEM over alloy 625 coupons is shown in Fig. 15. This figure represents the test results for both Solar_Salt_T and Solar_Salt_R mixtures during t_2 test time (1470 h). For both media, alloy 625 shows a seemingly homogeneous and well-adhered oxide layer of approximately 3 μm in the technical grade (Fig. 15a) and 1.5–2 μm in the refined grade (Fig. 15b). Intergranular corrosion and other localized phenomena are not observed for this material under test conditions. Magnesia crystals (MgO) are observed in the outermost zone of the oxide layer. Same conclusions regarding oxide layer thickness between different test times and test media extracted from 800H are also attributable to alloy 625.

3.4. Stress corrosion cracking and crevice corrosion evaluation

U-Bend specimens are descaled to remove oxides layer generated over the base metal for a better analysis of the alloys SCC susceptibility. Cracks are not detected in the bending areas of alloy 800H (Fig. 16a) and alloy 625 coupons (Fig. 16b) after t_2 test time exposure for both test fluids. Accordingly, both alloys do not show SCC susceptibility. In addition to SCC phenomena, corrosion crevice is also analyzed over the overlapping areas, not detecting any damage associated to this type of corrosion attack (Fig. 16c).

3.5. Corrosion rates calculus

Descaled weight losses and corrosion rates are calculated for alloy 800H and alloy 625 after being exposed to Solar_Salt_T and Solar_Salt_R mixtures following guidelines extracted from ASTM G1-03 (Table 4). Corrosion coupons tested during both test times, t_1 and t_2, are descaled and weighted after the termination of the tests. Furthermore, the alloy protection and passivation effect of the corrosion products generated over the base metal is discussed.

Alloy 800H shows corrosion rates decreasing with time for both nitrates mixtures, being Solar_Salt_T more aggressive than Solar_Salt_R.

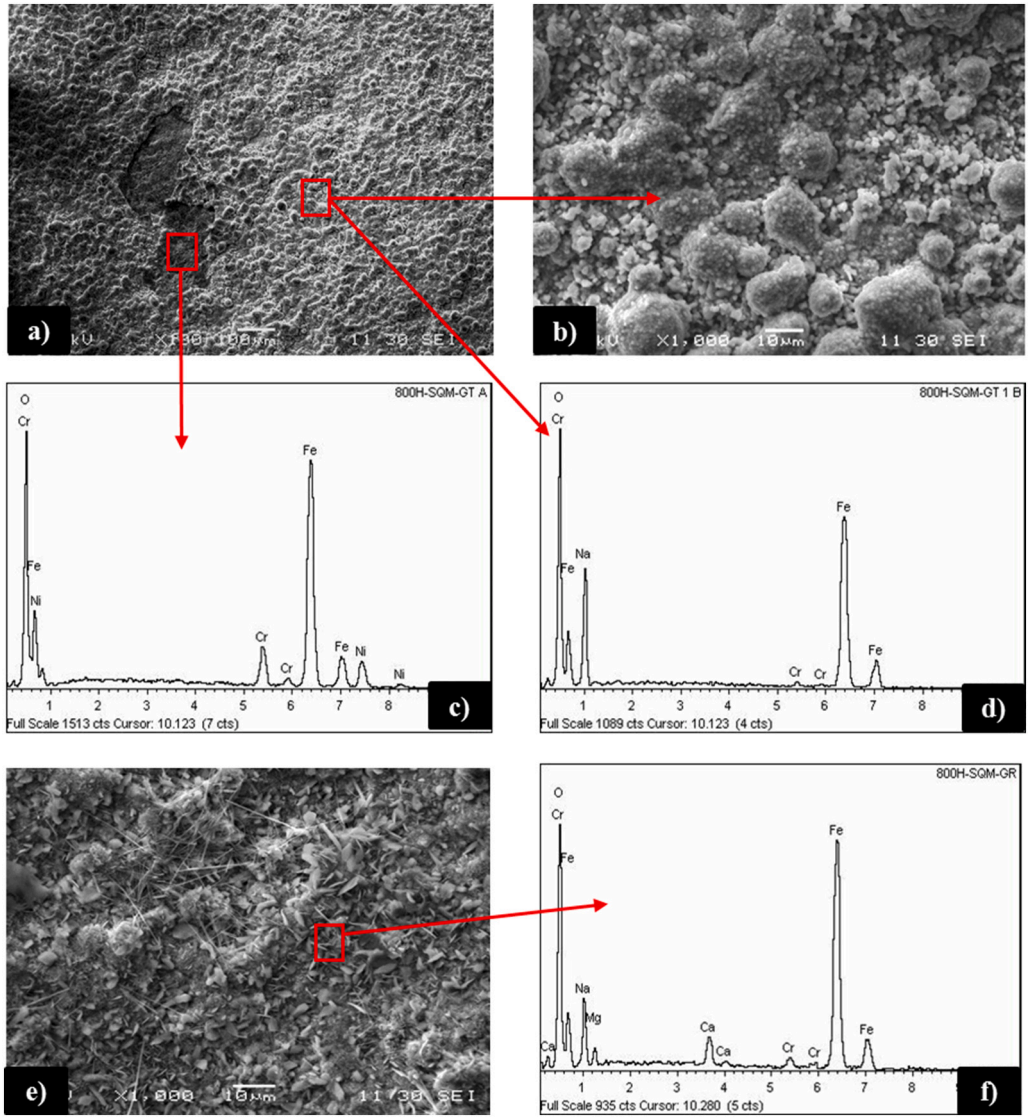

Fig. 10. Alloy 800H SEM micrograph and EDS spectra after t_2, 1470 h. (a) Alloy 800H coupon surface exposed to Solar_Salt_T; (b) Alloy 800H external oxide layer detail (Solar_Salt_T); (c) Alloy 800H inner oxide layer EDS spectrum (Solar_Salt_T); (d) Alloy 800H external oxide layer EDS spectrum (Solar_Salt_T); (e) Alloy 800H coupon surface exposed to Solar_Salt_R; (f) Alloy 800H oxide layer EDS spectrum (Solar_Salt_R).

Higher aggressiveness associated to Solar_Salt_T is linked to a higher level of impurities as displayed in Table 1. This result is in agreement with previous studies carried out by authors at lower temperatures [37]. Although some spalling phenomena are detected for coupons tested in Solar_Salt_T (Fig. 10a), alloy 800H generates oxides layers, which protect and passivate the alloy in both test fluids. This can be confirmed with the evolution of the corrosion rates over time (Table 4). Similar performance is detected for alloy 625 regarding corrosion rates evolution. Accordingly, corrosion rates measured after t_2 test time decreased regarding the ones calculated after t_1. In addition, exposure at Solar_Salt_T mixture produced a higher corrosion damage than Solar_Salt_R. Alloy 625 corrosion performance was better than alloy 800H for both test media under evaluation. In this way, alloy 800H corrosion rates are between 4.4 and 7.9 times higher than measured in alloy 625 for the different tests conditions exposed in Table 4. The excellent corrosion resistance observed in alloy 625 can be attributed to compact and well-adhered NiO oxide layer generated in the outermost corrosion products. As a conclusion, both alloys generate adherent oxides layers, which passivate the metal base against corrosion. This phenomenon is easily observable in Table 4, which analyze the tendency of weight loss and corrosion rate over time. Accordingly, it is expected that corrosion rates will decrease for long-term expositions, minimizing corrosion allowances needed to withstand 25 years of commercial operation from the corrosion point of view.

4. Conclusions

This study analyzes the corrosion performance of two different high strength materials, alloy 800H and alloy 625, proposed for the manufacturing of solar receivers in CSP plants using molten nitrate salts as heat transfer fluid and TES medium. Parameters such as test time and salt impurities are introduced in the tests matrix to analyze how the corrosion damage evolves through time, and quantify the effect of the salt grade in the corrosion performance of the alloys under evaluation.

Main conclusions extracted from the corrosion evaluation are as follow:

- Alloy 800H and alloy 625 coupons undergo uniform generalized corrosion after testing in Solar_Salt_T and Solar_Salt_R mixtures at 565 °C. Localized phenomena such as pitting, crevice corrosion and intergranular corrosion are not detected under the test conditions

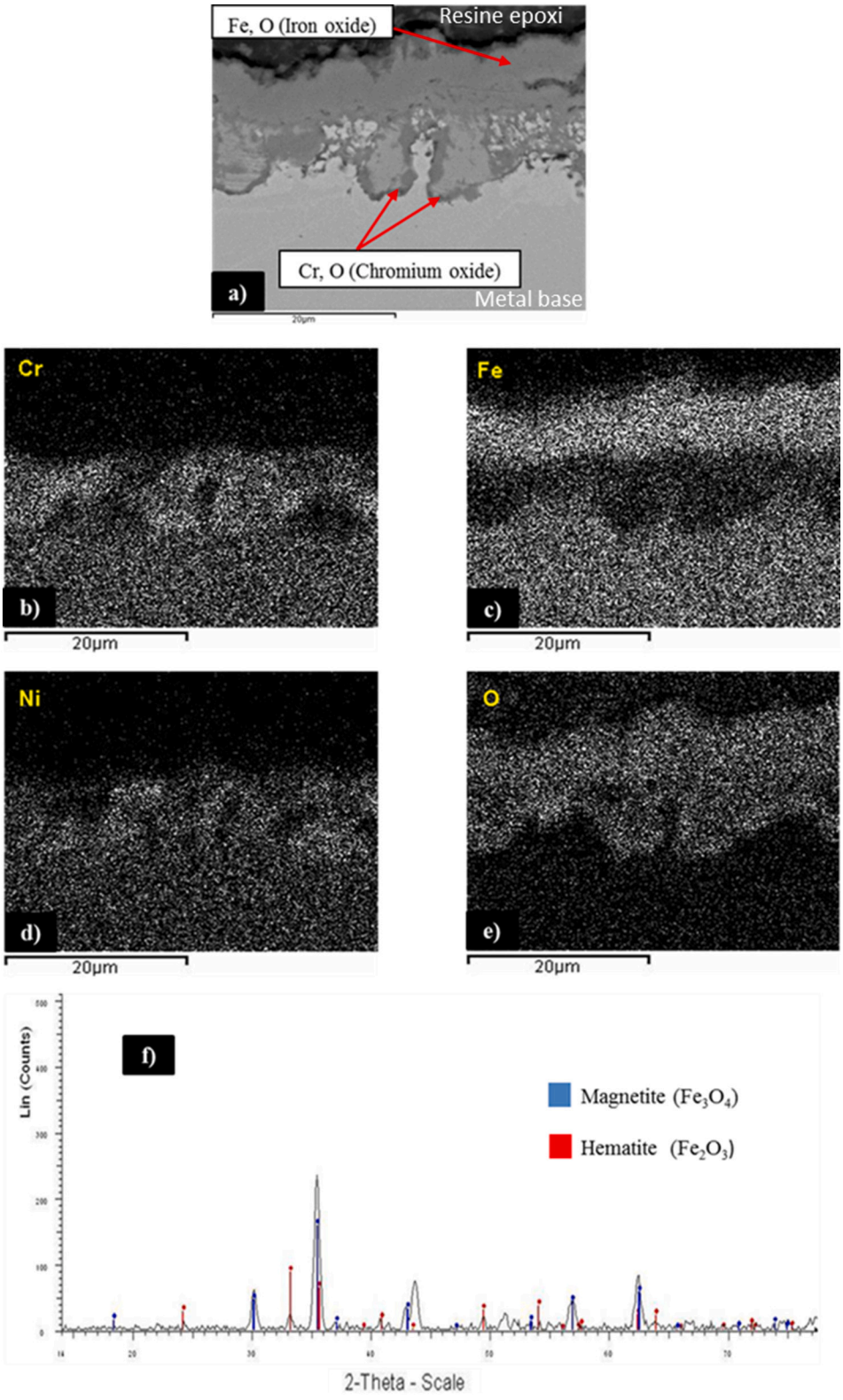

Fig. 11. Alloy 800H SEM-EDS mapping and XRD after 1470 h (Solar_Salt_T). (a) Alloy 800H micrograph detail; (b) EDS mapping: Cr distribution; (c) EDS mapping: Fe distribution; (d) EDS mapping: Ni distribution; (e) EDS mapping: O distribution; (f) Alloy 800H XRD spectrum.

executed in this study. Moreover, both alloys do not show SCC susceptibility by the U-bend method.

- Alloy 800H corrosion rates are higher than observed for alloy 625 at any test condition. Higher level of impurities associated to Solar_Salt_T provides a higher aggressiveness in terms of corrosion over both alloys. Corrosion rates measured for alloy 800H after t_2 test time are 32.4 µm/year and 52.9 µm/year for Solar_Salt_R and Solar_Salt_T respectively. On the other hand, alloy 625 corrosion rates are 7.4 µm/year (Solar_Salt_R) and 9.6 µm/year (Solar_Salt_T) after t_2 time exposure.

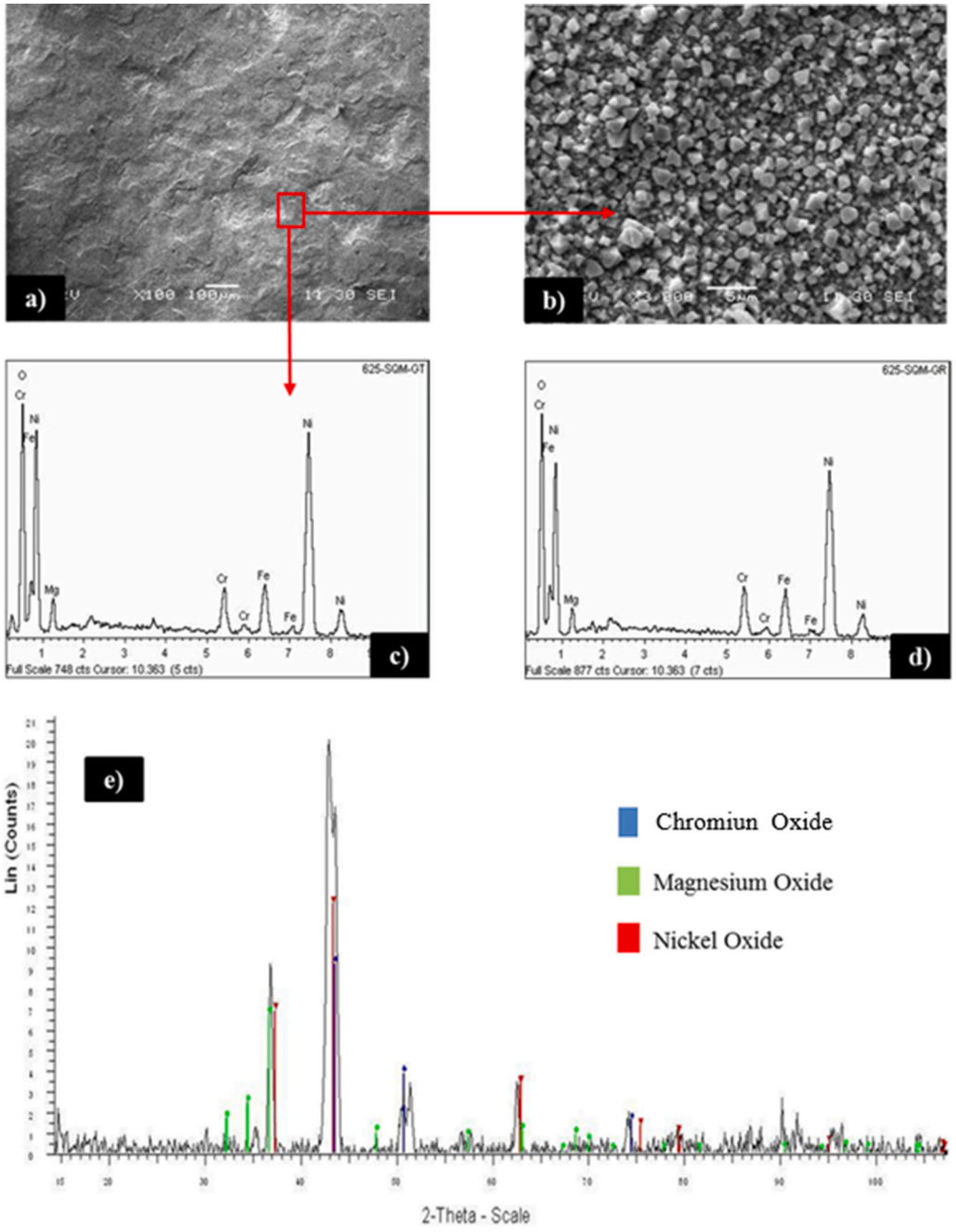

Fig. 12. Alloy 625 SEM surface analysis, EDS spectra and XRD evaluation after 1470 h. (a) Alloy 625 SEM micrograph detail, 100× (Solar_Salt_T); (b) Alloy 625 SEM micrograph detail, 3000× (Solar_Salt_T); (c) Alloy 625 EDS spectrum (Solar_Salt_T); (d) Alloy 625 EDS spectrum (Solar_Salt_R); (e) Alloy 625 XRD profile (Solar_Salt_T).

- Corrosion rate decreases progressively with exposure time due to protective layers generation over the surface of the metal alloy. Alloy 800H develops a duplex oxide layer consisting of iron oxides (Fe_2O_3 + Fe_3O_4) in its external part, and chromium oxide in its innermost layer. As the exposure time increases, the thickness of both the outer and the inner layer also increases. On the other hand, alloy 625 develops for both test fluids a fine, compact and highly adherent oxide layer consisting mainly of nickel oxide (NiO).

Summarizing, alloy 625 shows an excellent corrosion resistance with corrosion rates lower than 10 μm/year in any test condition due to the formation of a protective external NiO layer. Therefore, it is expected a promising long-term behavior in terms of corrosion for a molten salts solar receiver using alloy 625. On the other hand, although alloy 800H shows a lower corrosion resistance than alloy 625, corrosion attack morphology and corrosion rates evolution associated to alloy 800H also suggests a good corrosion performance for a long-term design. Taking into account that corrosion performance for alloy 800H and alloy 625 is acceptable for commercial applications, a detailed thermal-mechanical evaluation and cost analysis has to be carried out to identify the best candidate for the construction of solar receivers to be installed in MST facilities working at 565 °C.

CRediT authorship contribution statement

Cristina Prieto: Conceptualization, Methodology, Validation,

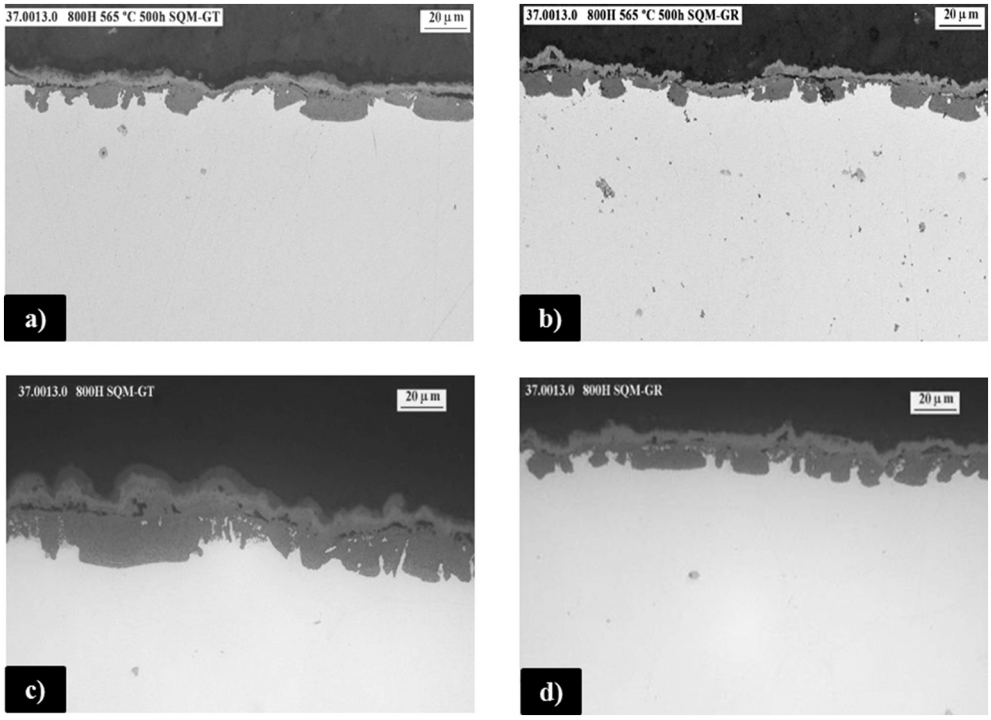

Fig. 13. Alloy 800H metallographic evaluation. (a) Alloy 800H exposed to Solar_Salt_T after t_1 test time; (b) Alloy 800H exposed to Solar_Salt_R after t_1 test time; (c) Alloy 800H exposed to Solar_Salt_T after t_2 test time; (d) Alloy 800H exposed to Solar_Salt_R after t_2 test time.

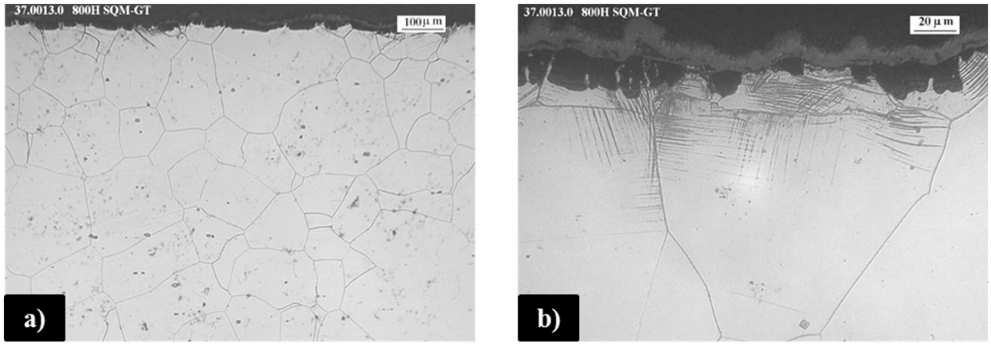

Fig. 14. Alloy 800H metallographic etching after t_2 exposure in Solar_Salt_T mixture. (a) Transversal section microstructure detail 1; (b) Transversal section microstructure detail 2.

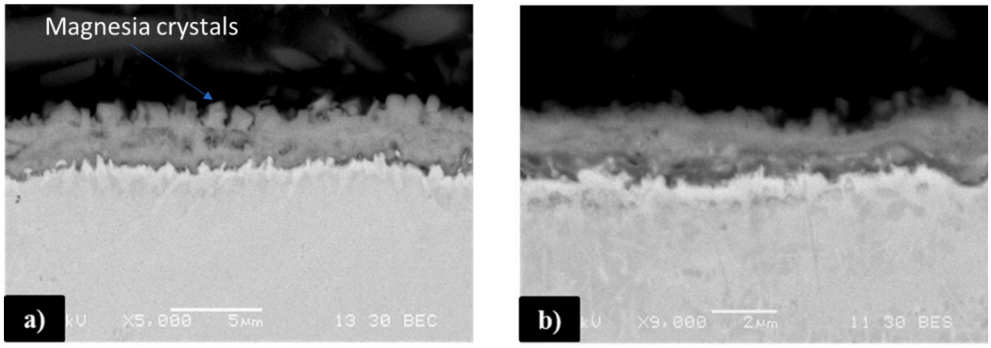

Fig. 15. Alloy 625 SEM micrograph after t_2 test time. (a) Alloy 625 coupon exposed to Solar_Salt_T mixture; (b) Alloy 625 coupon exposed to Solar_Salt_R mixture.

Resources, Data curation, Funding acquisition, Writing – original draft, Visualization, Supervision, Project administration. **F. Javier Ruiz-Cabañas:** Conceptualization, Methodology, Formal analysis, Investigation, Writing – original draft, Visualization. **Virginia Madina:** Methodology, Validation, Formal analysis, Investigation, Writing – review & editing. **Ana I. Fernández:** Validation, Investigation, Writing –

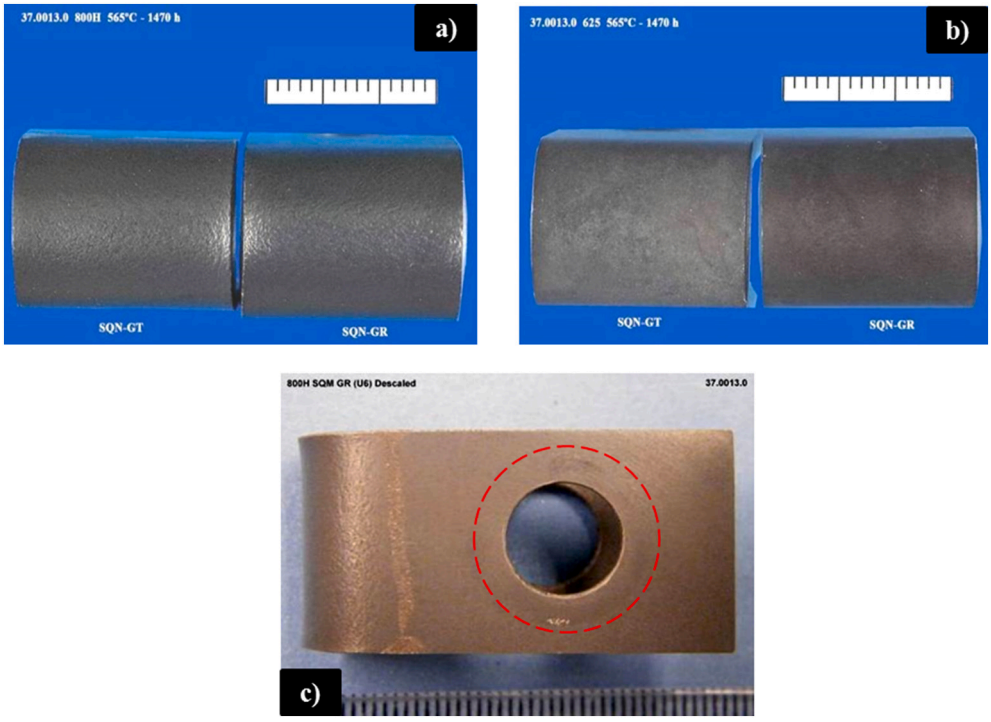

Fig. 16. SCC susceptibility and crevice corrosion attack evaluation after t_2 test time. (a) Alloy 800H U-bend specimens, Solar_Salt_T mixture (left) and Solar_Salt_R mixture (right); (b) Alloy 625 U-bend specimens, Solar_Salt_T mixture (left) and Solar_Salt_R mixture (right); (c) Alloy 800H crevice corrosion analysis detail (Solar_Salt_R mixture).

Table 4
Corrosion rates for alloy 800H and alloy 625 exposed to Solar_Salt_T and Solar_Salt_R after t_1 and t_2 test time.

Alloy	Fluid	Temperature (°C)	Test time (h)	Descaled weight loss (mg/cm^2)	Corrosion rate (μm/year)
Alloy 800H	Solar_Salt_T	565	1470	7.05	52.9 ± 1.1
		565	500	3.77	83.1 ± 2.3
	Solar_Salt_R	565	1470	4.32	32.4 ± 0.1
		565	500	3.29	72.6 ± 2.0
Alloy 625	Solar_Salt_T	565	1470	1.36	9.6 ± 0.9
		565	500	0.74	15.4 ± 1.2
	Solar_Salt_R	565	1470	1.05	7.4 ± 0.2
		565	500	0.44	9.2 ± 0.8

review & editing, Supervision. **Luisa F. Cabeza:** Validation, Resources, Writing – review & editing, Supervision, Project administration.

Declaration of competing interest

The authors declare that they have no known competing financial interests or personal relationships that could have appeared to influence the work reported in this paper.

Data availability

Data will be made available on request.

Acknowledgements

The research leading to these results has received funding from CENIT ConSOLida. This work was partially funded by the Ministerio de Ciencia, Innovación y Universidades de España (RTI2018-093849-B-C31 - MCIU/AEI/FEDER, UE and RTI2018-093849-B-C32 - MCIU/AEI/FEDER, UE) and by the Ministerio de Ciencia, Innovación y Universidades - Agencia Estatal de Investigación (AEI) (RED2018-102431-T). The authors from University of Lleida and University of Barcelona would like to thank the Catalan Government for the quality accreditation given to their research group GREiA (2017 SGR 1537) and research group DIOPMA (2017 SGR 138). GREiA and DIOPMA are certified agents TECNIO in the category of technology developers from the Government of Catalonia. This work is partially supported by ICREA under the ICREA Academia programme.

References

[1] IEA (International Energy Agency). World Energy Outlook Special Report 2015: Energy and Climate Change - Executive Summary.
[2] FAO (Food and Agriculture Organization), FAOSTAT: emissions - land use. http://faostat3.fao.org/faostat-gateway/go/to/download/G2/*/E, 2014. Accessed November 2018.
[3] IPCC (Intergovernental Panel on Climate Change), Mitigation of climate change: trends in stocks and flows of GHGs and their drivers. https://www.ipcc.ch/pdf/unfccc/sbsta40/SED/1_blanco_sed3.pdf, 2014. November 2018.
[4] Medium-term Renewable Energy Market Report, International Energy Agency (IEA), 2015. Accessed November 2018.
[5] L. Cabeza, E. Galindo, C. Prieto, C. Barreneche, A. Fernández, in: Key performance indicators in thermal energy storage:survey and assessment, 2015, pp. 820–827.
[6] A. Gil, M. Medrano, I. Martorell, A. Lázaro, P. Dolado, B. Zalba, L. Cabeza, State of the art on high temperature thermal energy storage for power generation. Part 1 - concepts, materials and modelization, Renew. Sustain. Energy Rev. 14 (2010) 31–55.
[7] S. Wagner, E. Rubin, Economic implications of thermal energy storage for concentrated solar thermal power, Renew. Energy 61 (2014) 81–95.

[8] J. Hernández-Moro, J.M. Martínez-Duart, CSP electricity cost evolution and grid parities based on the IEA roadmaps, Energy Policy 41 (2012) 184–192.
[9] Ko Nathanael, M. Lorenz, R. Horn, H. Krieg, M. Baumann, Sustainability assessment of Concentrated Solar Power (CSP) tower plants – integrating LCA, LCC and LCWE in one framework, Procedia CIRP 69 (2018) 395–400.
[10] V.M.B. Nunes, C.S. Queirós, M.J.V. Lourenço, F.J.V. Santos, C.A. Niesto de Castro, Appl. Energy 183 (2016) 603–611.
[11] C. Turchi, G. Heath, Molten Salt Power Tower Cost Model for the System Advisor Model (SAM). NREL/TP-5500-57625, National Renewable Energy Laboratory, 2013.
[12] E. González-Roubaud, D. Pérez-Osorio, C. Prieto, Review of commercial thermal energy storage in concentrated solar power plants: steam vs. Molten salts, Renew. Sustain. Energy Rev. 80 (2017) 133–148.
[13] L. Sena-Henderson, Advantages of Using Molten Salts, SANDIA National Laboratories, 2006.
[14] H.A. Najafabadi, N. Ozalp, An advanced modeling and experimental study to improve temperature uniformity of a solar receiver, Energy 165 (2018) 984–998.
[15] K.H. Clifford, Advances in central receivers for concentrating solar applications, Sol. Energy 152 (2017) 38–56.
[16] M.R. Rodríguez-Sánchez, C. Marugán-Cruz, A. Acosta-Iborra, D. Santana, Thermo-mechanical modelling of solar central receivers: effect of incident solar flux resolution, Sol. Energy 165 (2018) 43–54.
[17] G. Lay, High Temperature Corrosion And Materials Applications, ASM International, 2007.
[18] J.M. Lata, M. Rodríguez, M. Álvarez de la Lara, High flux central receivers of molten salts for the new generation of commercial stand-alone solar power plants, J. Sol. Energy Eng. 130 (2008) 21002.
[19] A.M. Kruizenga, D.D. Gill, M. LaFord, G. McConohy, Corrosion of High Temperature Alloys in Solar Salt at 400, 500, And 680°C (SAND 2013-8256), Sandia National Laboratories, 2013.
[20] A.M. Kruizenga, D.D. Gill, M. LaFord, Materials Corrosion of High Temperature Alloys Immersed in 600°C Binary Nitrate Salt (SAND 2013–2526), Sandia National Laboratories, 2013.
[21] K. Federsel, J. Wortmann, M. Ladenberger, High-temperature and corrosion behavior of nitrate nitrite molten salt mixtures regarding their application in concentrating solar power plants, Energy Procedia 69 (2015) 618–625.
[22] Y. Zhang, L. Xiao, J. Liu, M. Liu, M. Fu, Corrosion behavior of Incoloy 800 in molten nitrate salt, Adv. Mater. Res. 887–888 (2014) 357–361.
[23] R.W. Bradshaw, Thermal convection loop study of the corrosion of Incoloy 800 in molten NaNO3/KNO3, Corrosion 43 (1987) 173–178.
[24] M.R. Rodríguez-Sánchez, A. Sánchez-González, C. Marugán-Cruz, D. Santana, New designs of molten-salt tubular-receiver for solar power tower, Energy Procedia 49 (2014) 504–513.
[25] Z. Liao, X. Li, C. Xu, C. Chang, Z. Wang, Allowable flux density on a solar central receiver, Renew. Energy 62 (2014) 747–753.
[26] E. Setien, J. Fernández-Reche, M.J. Ariza-Camacho, M. Álvarez-de-Lara, Solar aging of receivers made of nickel super alloys, AIP Conf.Proc. 2033 (2018), 230012.
[27] C.K. Ho, B.D. Iverson, Review of high-temperature central receiver designs for concentrating solar power, Renew. Sustain. Energy Rev. 29 (2014) 835–846.
[28] C. Prieto, J. Gallardo-González, F.J. Ruiz-Cabañas, C. Barreneche, M. Martínez, M. Segarra, A.I. Fernández, Study of corrosion by dynamic gravimetric analysis (DGA) methodology. Influence of chloride content in solar salt, Sol. Energy Mater. Sol. Cells 157 (2016) 526–532.
[29] ASM Specialty Handbook: Nickel, Cobalt And Their alloys, ASM International, 2000.
[30] ASTM E112-13. Standard Test Methods for Determining Average Grain Size, ASTM International.
[31] S.H. Goods, R.W. Bradshaw, Corrosion resistance of stainless steels during thermal cycling in alkali nitrate molten salts, SAND2001-8518, 2001, https://doi.org/10.2172/1020472.
[32] S.H. Goods, R.W. Bradshaw, Corrosion of stainless steels and carbon steel by molten mixtures of commercial nitrate salts, J. Mater. Eng. Perform. 13 (2004) 78–87.
[33] ASTM G1-03. Standard practice for preparing, cleaning and evaluating corrosion test specimens, ASTM International.
[34] ASTM G30-95. Standard Practice for Making and Using U-Bend Stress-Corrosion Test Specimens, ASTM International.
[35] ASTM G78-01. Standard Guide for Crevice Corrosion Testing of Iron-Base and Nickel-Base Stainless Alloys in Seawater and Other Chloride-Containing Aqueous Environments, ASTM International.
[36] C. Prieto, F.J. Ruiz-Cabañas, A. Rodríguez-Sánchez, C. Rubio, A.I. Fernández, M. Martínez, E. Oró, L.F. Cabeza, Effect of the impurity magnesium nitrate in the thermal decomposition of the solar salt, Sol. Energy 192 (2018) 186–192.
[37] F.J. Ruiz-Cabañas, C. Prieto, V. Madina, A.I. Fernández, L.F. Cabeza, Materials selection for thermal energy storage systems in parabolic trough collector solar facilities using high chloride content nitrate salts, Sol. Energy Mater. Sol. Cells 163 (2017) 134–147.